Systematic variation of population receptive field properties across cortical depth in human visual cortex

Alessio Fracasso [a,b,c,*], Natalia Petridou [b,1], Serge O. Dumoulin [a,c,**,1]

[a] Experimental Psychology, Helmholtz Institute, Utrecht University, Utrecht, The Netherlands
[b] Radiology, Imaging Division, University Medical Center Utrecht, Utrecht, The Netherlands
[c] Spinoza Centre for Neuroimaging, Amsterdam, The Netherlands

ABSTRACT

Receptive fields (RFs) in visual cortex are organized in antagonistic, center-surround, configurations. RF properties change systematically across eccentricity and between visual field maps. However, it is unknown how center-surround configurations are organized in human visual cortex across lamina. We use sub-millimeter resolution functional MRI at 7 Tesla and population receptive field (pRF) modeling to investigate the pRF properties in primary visual cortex (V1) across cortical depth. pRF size varies according to a U-shaped function, indicating smaller pRF center size in the middle compared to superficial and deeper intra-cortical portions of V1, consistent with non-human primate neurophysiological measurements. Moreover, a similar U-shaped function is also observed for pRF surround size. However, pRF center-surround ratio remains constant across cortical depth. Simulations suggest that this pattern of results can be directly linked to the flow of signals across cortical depth, with the visual input reaching the middle of cortical depth and then spreading towards superficial and deeper layers of V1. Conversely, blood-oxygenation-level-dependent (BOLD) signal amplitude increases monotonically towards the pial surface, in line with the known vascular organization across cortical depth. Independent estimates of the haemodynamic response function (HRF) across cortical depth show that the center-surround pRF size estimates across cortical depth cannot be explained by variations in the full-width half maximum (FWHM) of the HRF.

© 2016 Elsevier Inc. All rights reserved.

Introduction

The visual cortex is organized at different spatial scales, ranging from microscopic (individual neurons) to mesoscopic (cortical columns and layers) and macroscopic (visual field maps and pathways) scales. Neurons within visual cortex process only a local extend of visual space: the classical receptive field (RF). The RFs are typically organized in an antagonistic fashion: the responses to stimulation in the classical RFs are modulated by stimulation in the extra-classical RF (or surround). These modulations can be excitatory or inhibitory and have been characterized in detail by electrophysiological and psychophysical studies

(Hubel and Wiesel, 1968; Allman et al., 1985; Cavanaugh et al., 2002). Furthermore, RF properties change systematically along the various spatial scales of the visual hierarchy.

Human functional magnetic resonance imaging (fMRI) can segregate the cortex into regions that contain separate maps of the visual field (Engel et al., 1994; Sereno et al., 1995; DeYoe et al., 1996). Recently, population receptive field (pRF) properties have been estimated using fMRI in humans (Dumoulin and Wandell, 2008; Kay et al., 2008). These pRF properties are estimated in degrees of visual angle and resemble those measured with neurophysiology, including suppressive surrounds (Zuiderbaan et al., 2012), and systematic changes within and between visual field maps (Dumoulin and Wandell, 2008; Amano et al., 2009; Winawer et al., 2010; Harvey and Dumoulin, 2011). Here we extend these measurements of antagonistic pRF properties to the mesoscopic scale using sub-millimeter resolution 7 Tesla fMRI and pRF modeling. Several recent studies investigated the laminar variation of blood-oxygenation-level-dependent (BOLD) signal in humans (Ress et al., 2007; Polimeni et al., 2010; Koopmans et al., 2010, 2011; Siero et al., 2011; Zimmermann et al., 2011; Olman et al., 2012; Chen et al., 2013; De Martino et al., 2013; Huber et al., 2014, 2015), non-human primates (Goense and Logothetis, 2006; Goense et al., 2007, 2012) and

* Correspondence to: A. Fracasso, Experimental Psychology, Helmholtz Institute, Utrecht University, Langeveld Gebouw, Heidelberglaan 1, Room H0.33, 3584 CS Utrecht, The Netherlands.
** Correspondence to: S. O. Dumoulin, Experimental Psychology, Helmholtz institute, Utrecht University, Langeveld Gebouw, Heidelberglaan 1, Room H0.54, 3584 CS Utrecht, The Netherlands.
E-mail addresses: A.Fracasso@uu.nl (A. Fracasso), S.O.Dumoulin@uu.nl (S.O. Dumoulin).
[1] Equal contribution.

other mammals (Silva and Koretsky, 2002; Harel et al., 2006; Jin and Kim, 2008), but none of the aforementioned studies investigated the cortical depth dependence of pRF properties.

The cortex is divided into six functionally and structurally distinct layers. In primary visual cortex (V1), information arrives indirectly from the retina through afferents from the lateral geniculate nucleus (LGN), and enters the cortex mainly (but not exclusively) in layer 4 (granular layer, Sincich and Horton, 2005). After the first synapse in the granular layer, information rapidly spreads along cortical depth towards supra- and infra-granular layers (Self et al., 2013). The local neural circuitry across this layered structure underlies crucial stages in early visual processing, as the functions of extra-striate visual cortical areas receiving input from V1 are based on the patterns generated in V1 (Callaway, 1998).

It is unknown how the size of center-surround configurations is organized in human V1 across lamina. Using invasive neurophysiology, neural RF sizes vary across cortical layers in rat somatosensory and visual cortex (Chapin, 1986; Vaiceliunaite et al., 2013; Self et al., 2014). On the other hand, in macaque V1 how RF sizes vary across cortical layers is not as clear cut. Hubel and Wiesel (1972, 1977) point out that there is a correlation between complexity and layering, where the cells in layer IV tend to be least complex with smaller RFs. On the other hand, Sceniak et al. (2001) and Shushruth et al. (2009) report approximately constant RF sizes across lamina except for larger RF sizes in layer 6. Sceniak and colleagues also report surround suppression greatest in layer 4B and weakest in layer 6, whereas others report that far surrounds are larger outside input layer 4 (Shushruth et al., 2009; Angelucci et al., 2002).

Here we estimate the size of center-surround configurations across cortical depth in human V1. We demonstrate systematic and balanced center-surround changes across cortical depth. These changes cannot be explained by variations of the haemodynamic response properties. These results extend our knowledge on pRF properties in early visual cortex, showing that their change is not limited across eccentricity and visual field map hierarchy (Dumoulin and Wandell, 2008), but also extends across cortical depth, suggesting a balanced center-surround relationship within the laminar hierarchy.

Methods

Participants

Four males participated in the experiment (age range 30–40 years). Two participants were naïve to the experiment purpose. All participants have normal or corrected-to-normal visual acuity. All experimental procedures were conducted in accordance with the ethical standards laid down in the 1964 Declaration of Helsinki (most recently amended in 2008, Seoul), and cleared by the ethics committee of the University Medical Center Utrecht.

Visual stimuli setup

Visual stimuli were presented by back-projection onto a 15.0 × 7.9 cm screen inside the MRI bore. Participants viewed the display through prisms and mirrors, and the total distance from the participant's eyes (in the scanner) to the display screen was 35 cm. Display resolution was 1024 × 538 pixels. The stimuli were generated in Matlab (Mathworks, Natick, MA, USA) using the PsychToolbox (Brainard, 1997; Pelli, 1997).

V1 definition and pRF modeling at conventional resolution

The primary visual cortex field map was reconstructed using near-identical procedures as in previous studies (Dumoulin and Wandell, 2008; Amano et al., 2009; Winawer et al., 2010; Harvey and Dumoulin, 2011). Stimuli consisted of drifting bar apertures at four orientations, which exposed a checkerboard pattern moving parallel to the bar orientation (Dumoulin and Wandell, 2008). Alternating rows of checks moved in opposite directions, and orthogonally with respect to the bar orientation. The bar width (and width of alternating white and black checks) subtended one-quarter of the stimulus radius (1.56 degrees of visual angle). The bar moved across the stimulus aperture in 20 evenly spaced steps, each 0.625 degrees of visual angle, 1/20th of the stimulus window diameter. As there was one step at the start of each functional volume acquisition, each pass of the stimulus lasted for 20 acquisition repetitions (TRs), 30 s. Four bar orientations and two different motion directions for each bar were presented, giving a total of eight bar motion directions (upward, downward, left, right, and four diagonals) within each run (the same stimuli order was presented for each run). After each horizontal or vertical bar orientation pass, a 30 s of mean-luminance (zero contrast) stimulus was displayed. Four mean-luminance blocks were presented at regular intervals during the scan. Participants fixated on a dot in the center of the visual stimulus. The model estimates a pRF for every voxel using a method previously described (Dumoulin and Wandell, 2008). We used the position estimates of the pRF to define V1. Area V1 was defined on T1-weighted anatomical MRI data with a voxel size of 0.8 × 0.8 × 0.8 mm (resampled at 1 mm isotropic). Repetition time (TR) was 7 ms, echo time (TE) was 2.84 ms and flip angle was 8°. Functional T2*-weighted multi-slice echo-planar images (EPIs) were acquired using a Philips Achieva 7 T scanner (Best, Netherlands), a volume transmit coil for excitation and a 32-channel head coil for signal reception (Nova Medical, MA, USA). Acquisition parameters were: TR/TE: 1500/30 ms, flip angle: 70°, voxel size: 2 mm isotropic, and 24 coronal slices. Functional scans were each 248 time frames (372 s) in duration, and the first eight time frames were discarded to ensure that signal had reached steady state.

PRF estimation across cortical depth: Visual stimuli and imaging

Sub-millimeter functional imaging is characterized by relatively slow repetition time (TR = 4 s in our experiment, see methods below). This limited the number of time-points available in our time-series (72 time points for each time-series, see methods below). Due to this limitation, we aimed to keep the number of parameters estimated from each time-series at minimum, in order to maximize the number of degrees of freedom at the modeling stage. To this aim, the visual stimuli used to map pRF across cortical depth consisted of an expanding and a contracting ring aperture (Fig. 1A), which exposed a checkerboard pattern moving radially (Dumoulin and Wandell, 2008). Using this stimulus, for each ring step at a given eccentricity and TR, we stimulate all pRFs at that specific eccentricity. This allows us to estimate 3 main parameters: the optimal eccentricity, center pRF size and surround pRF size for each responsive voxel, instead of the 4 main parameters usually derived from pRF modeling: optimal × position, y position, center pRF size and surround pRF size.

Alternating rows of checks moved in opposite directions. The ring width subtended 0.5 degrees of visual angle and moved across the stimulus aperture in 12 evenly spaced steps, each 0.25 degrees of visual angle (Fig. 1A). Each pass of the stimulus lasted for 12 acquisition repetitions (TRs), 48 s. Two different ring directions were presented (expanding and contracting). After each expanding or contracting ring pass, 20 s of mean-luminance (zero contrast) stimulus was displayed. The stimulation sequence for each run was as follows: expanding ring–contracting ring–contracting ring–expanding ring, with each single part of the stimulation sequence intermixed with the baseline condition (Fig. 1B). Participants were asked to fixate a dot in the center of the visual stimulus and report colour changes; mean performance across runs and participants was 85%.

High resolution functional data were acquired using the 7 T scanner (Philips, Best, Netherlands), and the volume transmit coil for excitation

(Nova Medical, MA, USA). Head motion inside the scanner was minimized using a combination of noise-cancelling headphones and foam padding. Functional T2*-weighted 3-dimensional multi-shot EPI (3D-EPI, two shots per slice, 35 slices, 70 shots overall) data were acquired using two custom-built high-density 16-channel surface coils (total 32 channels) for signal reception (Petridou et al., 2013). The sequence parameters were: TR/TE = 57/28 ms, flip angle: 20°, acceleration factor using SENSE encoding: 3.5 (right-left) × 1.3 (anterior-posterior), echo planar factor: 27, BW (phase-encode): 19.1 Hz/pixel, readout duration ~52 ms (with potential blurring in the phase-encode direction estimated at ~16%) (Haacke et al., 1999), voxel size = 0.70 mm isotropic, FOV = 131 (right-left) × 120 (feet-head) × 24.5 (anterior-posterior) mm³, 35 coronal slices, and 28% oversampling in the slice direction. Functional volumes were acquired every 4 s and functional scans were each 72 time frames (288 s) in duration. Each participant participated in 6 to 9 runs, on a single session.

HRF estimation across cortical depth: Visual stimuli and imaging

On a separate session, two functional scans were acquired for each participant using an event-related paradigm design consisting of 306 s. The stimuli sequence was generated with interstimulus intervals (ISIs) taken from a uniform distribution between 2.55 s and 10.2 s (Burock et al., 1998; Hagberg et al., 2001), and a mean ISI of 8.28 s. In total, 44 stimuli were presented with a stimulus duration of 850 ms (two full-field opposing checkerboard frames of 425 ms each, size = 9 × 9 degrees of visual angle). Short stimuli together with an ISI of at least 2.55 s will yield a narrow HRF, decreasing the chances of hemodynamic nonlinearities (Miezin et al., 2000; Pfeuffer et al., 2003; Zhang et al., 2008). Participants were asked to fixate a dot in the center of the visual stimulus and report colour changes; mean performance across runs and participants was 78%.

Functional data were acquired using the scanner setup described above. Acquisition parameters were: T2*-weighted single-shot multi-slice EPI with: TR/TE = 850 ms/27 ms, acceleration factor using SENSE encoding: 3.1 (right-left), flip angle: 50°, resolution = 1.3 mm isotropic, 13 coronal slices, FOV = 160 × 130 mm². Functional scans were each 360 time frames (306 s) in duration. Each participant participated in 2 runs, on a single session. High temporal resolution cardiac and respiratory rate data were recorded during all scans for all subjects by means of a laser finger-clip and a belt placed around the upper abdomen, respectively. Both high resolution functional acquisitions (for pRF and HRF estimation) were centered on the occipital pole of each participant, around the calcarine fissure. HRF was also estimated using the 3D-EPI sequence (4 s TR), using a similar paradigm as the one adopted for the 2D-EPI sequence, by increasing the delay between visual stimuli. The stimuli sequence was generated with interstimulus intervals (ISIs) taken from a uniform distribution between 5 s, 9 s and 3 s. In total, 36 stimuli were presented with a stimulus duration of 850 ms (two full-field opposing checkerboard frames of 425 ms each, size = 9 × 9 degrees of visual angle).

Preprocessing of high resolution functional data

fMRI analysis was performed in the mrVista software package for MATLAB, which is freely available at (http://white.stanford.edu/software/), and the software Slicer (Fedorov et al., 2012, http://www.slicer.org/). For computation of the head movement between scans, the first functional volumes for each scan were aligned (Nestares and Heeger, 2000). Within scan motion correction was computed by aligning the frames of a scan to the first frame. Motion corrected volumes were averaged together to increase signal-to-noise ratio. For each participant, V1 was identified from the independent pRF mapping scan (see details in the V1 definition and pRF modeling at conventional resolution section). The 1 mm isotropic structural scan where V1 was identified was realigned to the functional scans using 6 degrees of freedom. The analysis was limited to each participant's V1.

Gray and white matter segmentation

An accurate gray matter (GM)/white matter (WM) segmentation is critical when the aim is to characterize activity across the cortical depth. Specifically, the key issues are misalignment between the functional and anatomical volumes due to local geometric distortions, and a decreased resolution due to interpolation that is necessary to do this alignment. The analysis is limited to V1, which is located at the center of the field of view. The geometric distortions in this central location of the FOV are minimal compared to those at the borders of the acquired volume. Furthermore, we used a new approach that took advantage of recent evidence showing that T2*-weighted phase images can reveal considerable detail of anatomical structure in the human brain (Abduljalil et al., 2003; Haacke et al., 2004; Duyn et al., 2007; Petridou et al., 2010). We capitalized on this enhanced contrast to perform the segmentations directly on the T2*-weighted 3D-EPI functional acquisitions (Fig. 2). Thus the GM/WM segmentation was performed manually for each participant and directly on the functional 3D-EPI space at the original acquisition resolution. This approach avoids the key issues of misalignment and interpolation mentioned above, and takes into account geometric distortions as much as possible by directly building our distance map within this space.

Motion corrected 3D-EPI volumes across all scans were averaged together to obtain a mean 3D-EPI amplitude volume (Fig. 2A). A brain mask was created using BET (Jenkinson et al., 2012) and applied to raw phase images. Phase images were unwrapped using an approach already adopted by others using Laplacian unwrapping and SHARP filtering (Bilgic et al., 2014). The unwrapped phase images were motion corrected using the motion parameters obtained from the 3D-EPI amplitude images (Nestares and Heeger, 2000; Petridou et al., 2010) and averaged together to increase the signal to noise ratio and obtain a mean 3D-EPI phase volume (Fig. 2B). The mean amplitude and mean phase volumes were weighted (70% mean phase and 30% mean amplitude, Fig. 2C) and superimposed using Slicer (Fig. 2C) and used as a starting point for manual segmentation of the entire EPI volume, on a single participant basis (Fig. 2D).

This segmentation served as a basis to compute the cortical depth distance map needed to identify the location of each voxel in the 3D-EPI space with respect to the GM/WM border.

We are aware that GM/WM segmentation directly on the EPI space is potentially prone to error. We provide validation of the accuracy of this segmentation by comparing against the segmentation performed on a high resolution anatomical T1-weighted scan (Fracasso et al., 2016; see Supplementary material, Figs. 1 & 2), showing a good correspondence between segmentations obtained from T1-weighted images and from the images in the 3D-EPI space.

Cortical depth map

Starting from the manual segmentation in the 3D-EPI space, 3D meshes were derived from the GM/WM border. For this purpose, the segmented volume was smoothed using a Gaussian kernel (sd = 0.4 mm) and thresholded. This step was included to build a smoother 3D mesh of the GM/WM surface. A precise depth map was calculated between each voxel and the vertices of the GM/WM mesh surface. For each voxel, the smallest Euclidean distance to any vertex on that surface was computed. White matter locations were assigned a negative depth value. We adopted Euclidean distance as a metric to identify voxels in gray matter, as done in previous laminar imaging studies (Ress et al., 2007). Recently, it has been shown that the optimal metric to identify the stria of Gennari in primary visual cortex (i.e. optimal metric to identify voxels in gray matter) differs from the Euclidean distance (Equivolume metric, Waehnert et al., 2014). However, consistent

improvements in metric definition are found for extremely high resolutions (~0.15 mm isotropic), whereas the metric outcomes are indistinguishable for relatively lower resolutions (0.7 mm isotropic, as in this case, Waehnert et al., 2014).

pRF modeling across cortical depth

The linear trend of each voxel time series was removed and the resulting time series were normalized by their mean amplitude over time to obtain a %BOLD response.

pRF sizes and eccentricities were estimated from the data of each voxel using a forward model derived by the stimuli sequence (Dumoulin and Wandell, 2008). The BOLD response of each voxel was predicted using a one-dimensional difference of Gaussian (DoG) pRF model (Zuiderbaan et al., 2012). This modeled each voxel's response as a function of spread and eccentricity at a given position. The predicted fMRI time course was calculated by convolution of the modeled pRF, the stimulus sequence, and a canonical BOLD hemodynamic response function (Friston et al., 1998; Glover, 1999, FWHM = 5.3 s). The DoG pRF model was defined as the combination of two separate Gaussians (a first Gaussian for the excitatory pRF center and a second Gaussian for the inhibitory pRF surround) plus the DC component. The center (excitatory) pRF size, surround (inhibitory) pRF size, and eccentricity for each voxel were determined by minimizing the sum of squared errors (RSS) between the predicted and observed fMRI time series. At the fit stage, the DC component and scaling factors of the best GLM fit were stored to obtain an estimate %BOLD response amplitude as well as R^2 goodness of fit value per voxel.

Voxels in the functional 3D-EPI space were selected according to three different criteria: (i) only voxels in V1 (defined from the independent session, see the V1 definition and pRF modeling at conventional resolution section) were analyzed. (ii) Analysis was limited to those voxels where Euclidean distance from the GM/WM surface was between 0 and 2.5 mm. (iii) Analysis was limited to those voxels where R^2 exceeded the 75% quantile at the single subject level (mean R^2 across participants = 55% ± 14%). After applying the above criteria, 3564, 2287, 2807 and 3249 voxels entered the subsequent pRF analysis across cortical depth, for each of the four participants respectively.

pRF size scales linearly with eccentricity across V1 (Dumoulin and Wandell, 2008). To account for the eccentricity covariate, selected voxels were binned in 10 bins according to 10% percentiles of Euclidean distance from GM/WM surface. For each separate Euclidean distance bin, the eccentricity estimate was binned in 10 points (according to 10% percentiles of eccentricity). Mean pRF size was computed for each eccentricity point (Fig. 3) and the pRF × eccentricity linear relation was fit using standard GLM in order to derive the line equation estimating the intercept and the slope. For each bin we then obtained an estimate of pRF size versus eccentricity intercept and slope. Given that our stimuli covered ~4 degrees of visual angle, radius, for each bin we estimated pRF size at the eccentricity of 2°, by solving:

$$pRF_{estimate} = pRF_{intercept} + pRF_{slope} * 2 \qquad (1)$$

the pRF size at an eccentricity of 2° visual angle was taken as the pRF size estimate for the corresponding Euclidean distance bin (different examples of the linear fit at different depths are reported in Fig. 3). The 10 pRF size estimates across the Euclidean distance bins constituted the pRF size profile across cortical depth. The pRF profile across cortical depth was fit using a fourth order polynomial to extract the general shape of the profile.

Local minima in the profile were estimated by extracting the first zero-crossing point of the first derivative of the polynomial fit, if it existed. For the same bins, mean %BOLD signal change was computed to obtain the %BOLD profile across cortical depth. Furthermore, we measured the influence of the suppressive surround on the center pRF, by adapting a measure already adopted in Sceniak et al. (2001) by using the formula:

$$SI = \frac{\beta_{surround} * \sigma^2_{surround}}{\beta_{center} * \sigma^2_{center}}. \qquad (2)$$

This expression gives an index of suppression strength that varies between 0 and 1. A value of 0 indicates no suppression whereas 1 indicates suppression equal in strength to that of excitation in the center.

The 95% confidence interval (CI) of the center and surround pRF size estimates, local minimum, %BOLD, and suppression index estimates of the cortical depth profiles, was computed on a single participant basis, by 2000 bootstrapped samples, with replacement.

Simulating our accuracy to distinguish pRF sizes

Our aim was to obtain an estimate of the range of possible pRF sizes that could be reliably estimated. Results from the literature suggest that differences between pRF sizes across cortical depth are in the range of 30%–40% (Chapin, 1986; Sceniak et al., 2001). The precision with which pRF size can be measured with fMRI depends on a number of elements, among which neuronal scatter (a measure of positional variance of neurons, coding spatial positions at the same eccentricity level, Hetherington and Swindale, 1999), the visual stimuli, and the number of data-points available in the time series. These last two elements are of crucial importance since they are directly under experimental control. In this investigation the ring width subtended 0.5 degrees of visual angle and moved across the stimulus aperture in 12 evenly spaced steps, each 0.25 degrees of visual angle, hence each step was superimposed with the previous by 0.25 degrees of visual angle. Our aim was to obtain an estimate of the range of possible pRF sizes that could be reliably estimated, given the number of time frames in the time course (72), at a single voxel level. We simulated 2 noise-free time series starting from 2 separate pRFs: one with size α and a second one with size α(1 − Δ_α). Another 2 time series were generated adding an independent and identically distributed (i.i.d.) random noise component to the noise-free time series (noise-added), in order to match an expected mean variance explained of 50% (as obtained in our data). This procedure gave a total of 4 time series: 2 noise-free and 2 noise-added (adding i.i.d. noise, see Fig. 4, panels A & B). The variance explained by each noise-free series over each noise added time series was computed giving a total of 4 variance explained values: 2 matching variance explained values (noise-free α over noise-added α or noise-free α(1 − Δ_α) over noise-added α(1 − Δ_α)) and 2 non-matching variance explained values (noise-free α over noise-added α(1 − Δ_α) or noise-free α(1 − Δ_α) over noise-added α). If the matching variance explained was larger than the non-matching variance explained, then the technique could correctly assign each pRF size estimate to each noise-added time series, otherwise the estimates would be confounded, showing the limit of the estimation technique.

In the simulation, the parameter α was allowed to vary between 0.2 degrees of visual angle and 6 degrees of visual angle (based on pRF full width half max), the parameter 1 − Δ_α was allowed to vary between 0.1 (10%) and 0.9 (90%). In this way we could estimate the range of degrees of visual angle over which we could reliably estimate a given standard pRF size (the parameter α) for a range of pRF size differences with respect to the standard (the parameter 1 − Δ_α), at the single voxel level.

Simulation results show that, given the visual stimulation condition adopted in the experiment, we can reliably differentiate one pRF ranging between ~0.4 degrees of visual angle and ~4 degrees of visual angle, from a second pRF that is 30% smaller than the former (1 − Δα = 0.3), a range compatible with existing literature (Fig. 4C). The sensitivity of the pRF size estimation adopted decreased dramatically when the size of the second pRF was too close to the size of the first pRF (only 10% smaller, 1 − Δ_α = 0.1, Fig. 4D). This simulation suggests that we can reach a level of precision in pRF size estimation that is

compatible with the pRF size range across cortical depth reported in literature, at the single voxel level (Sceniak et al., 2001, Fig. 4C).

HRF estimation across cortical depth

The T2*-weighted single-shot multi-slice EPI functional scans (see the HRF estimation across cortical depth: Visual stimuli and imaging section) were corrected for motion and linear drift, and then corrected for cardiac and respiratory fluctuations using RETROICOR (Glover et al., 2000). For each voxel, the signal was normalized with respect to the mean signal across the whole time-series to obtain %BOLD signal change. Estimation of the HRF was performed using AFNI (http://afni.nimh.nih.gov/) by modeling the HRF for each voxel as a weighted linear sum of a set of triangular functions (TENT functions). 16 datapoints were estimated, spanning from 0 (stimuli onset time) to 13.6 s after stimulus onset time. Voxels were selected according to three different criteria: (i) V1 voxels were selected based on the independent scan (see the V1 definition and pRF modeling at conventional resolution section). (ii) Analysis was limited to those voxels where Euclidean distance from the GM/WM border was between 0 and 2.5 mm, and (iii) analysis was limited to those voxels that responded to the visual stimulation ($p < 0.001$, FDR corrected). Selected voxels were binned in 5 points according to 20% percentiles of Euclidean distance, for each bin the mean HRF was computed. From the mean HRF, two parameters were estimated: amplitude (max %BOLD response of the HRF) and full-width at half maximum (FWHM). The same analysis was used to estimate HRF parameters using the 3D-EPI sequence, but in this case the signal from each voxel was upsampled to a temporal resolution of 0.85 s by means of linear interpolation, to match the 2D-EPI acquisition.

Results

BOLD responses differ across cortical depth

Typical time series from single voxels are illustrated in the three panels of Fig. 5, demonstrating that single time-courses change across cortical depth, in particular that signal amplitude (%BOLD) increases towards the pial surface.

Moreover, the width of the response also changes. We summarized the time-series by deriving the pRF parameters and %BOLD signal change (insets), and observe smaller pRF sizes located in between the GM/WM border and the pial surface. These time series are selected at different cortical depths at comparable eccentricities, so changes in pRF properties cannot be ascribed to changes in eccentricity. Next we quantify these observations by averaging pRF parameters as a function of cortical depth.

PRF properties vary systematically across cortical depth

pRF center and surround estimates scale linearly with eccentricity (Fig. 6A, see Table 1), as it is commonly reported in neurophysiology and fMRI studies (Felleman and Van Essen, 1987; Dumoulin and Wandell, 2008; Kay et al., 2008). Single participant statistics for the slope and intercept parameters are reported in the following table:

In order to extract cortical depth profiles, we determine the pRF properties at 2 degrees of visual angle eccentricity. Cortical depth profiles of pRF center size show a U-shaped function with smaller

pRF size in the middle of cortical depth compared to superficial and deeper intra-cortical portions in V1 (Fig. 6B). The same trend is also present for pRF surround size estimates (Fig. 6C). Local minimum and the 95% confidence interval of center and surround U-shaped function estimates for each participant are reported in the following table, (Table 2):

On the other hand, suppression index (see Eq. (2)) remains flat across cortical depth, indicating that the ratio of center and surround does not change across cortical depth (Fig. 6D).

Theoretically, the voxel selection criteria (see the pRF modeling across cortical depth section, only voxels above the 75% R^2 quantile were included in the analysis) could introduce a sampling bias towards the pial surface, given that %BOLD signal increases towards the pial surface. However by inspecting the distribution of cortical depth estimates, we observe that it is only slightly affected by the sampling (see Supplementary material, Figs. 3 and 4). Moreover, the profiles across cortical depth are based upon 10% percentiles of cortical depth from the GM/WM border, so each point in the plot comes from the same number of voxels on each bin.

Results are consistent across participants (Fig. 7, solid lines). Data from one participant was split into two sets (runs 1–4 and runs 5–9) and each set was analyzed separately to assess the robustness of the results. Results are consistent across the two sets (Fig. 7, dashed lines). Given the results of our simulation (Fig. 4), the observed size estimates of ~0.8 degree of visual angle for pRF center (Fig. 7A) and ~2.7 degrees of visual angle for pRF surround (Fig. 7B) are well within the sensitivity boundaries of the adopted technique and are likely to reflect the real estimate of the underlying neuronal population rather than just an artifact due to the limits of the technique, such as ceiling or floor effects. Mean pRF center (Fig. 7A) and surround profiles (Fig. 7B) show a significant quadratic trend with respect to cortical depth ($t = 5.95$, $p = 0.0006$ and $t = 9.77$ and $p < 0.0006$, respectively). Suppression index remains flat across cortical depth (Fig. 7C, slope parameter for a linear model with respect to cortical depth does not significantly depart from zero, $t = -1.83$, $p = 0.11$).

HRF properties cannot explain pRF changes across cortical depth

The HRF also changes systematically across cortical depth. However, HRF parameters increase monotonically towards the pial surface, as previously reported (Siero et al., 2011), unlike the U-shaped profiles of pRF size across cortical depth. Nevertheless, we measured the HRF properties in the same subjects. We found a monotonic increase in %BOLD signal change amplitude as captured by the pRF analysis (Fig. 8A, linear model slope parameter: $t = 9.72$, $p < 0.0001$), as reported in previous studies (De Martino et al., 2013; Koopmans et al., 2011; Polimeni et al., 2010). During an independent scanning session we confirmed that both the HRF amplitude (Fig. 8B, linear model slope parameter: $t = 6.15$, $p = 0.008$) and FWHM (Fig. 8C, linear model slope parameter: $t = 17.92$, $p = 0.0003$) increase monotonically towards the cortical surface. Therefore, the profile of pRF properties across cortical depth cannot be explained by systematic changes of HRF parameters across cortical depth.

The HRF measurements were performed using a 2D EPI sequence whereas the main data were acquired using a 3D EPI sequence. It is possible that the HRF differed slightly between the two acquisition

Table 1
Single participant statistics for the slope and intercept parameters, for the pRF size × eccentricity relation.

	pRF center, intercept	pRF center, slope	pRF surround, intercept	pRF surround, slope
Participant 1	$t = 13.53$, $p < 0.0001$	$t = 7.05$, $p < 0.0001$	$t = 8.52$, $p < 0.0001$	$t = 7.38$, $p < 0.0001$
Participant 2	$t = 10.11$, $p < 0.0001$	$t = 3.09$, $p = 0.010$	$t = 6.63$, $p < 0.0001$	$t = 4.08$, $p = 0.003$
Participant 3	$t = 5.46$, $p = 0.0006$	$t = 2.14$, $p = 0.06$	$t = 5.37$, $p < 0.0001$	$t = 3.38$, $p = 0.009$
Participant 4	$t = 9.086$, $p < 0.0001$	$t = 5.46$, $p = 0.0004$	$t = 6.14$, $p < 0.0001$	$t = 4.03$, $p = 0.003$

Table 2
Local minimum and 95% confidence interval of center and surround U-shaped function estimates for each participant are reported in millimeters from the GM/WM boundary. Linear and quadratic trends on pRF center and surround across cortical depth were tested sequentially. The R^2 for the linear and linear + quadratic trends are reported, together with the ANOVA test on the comparison between the model including the linear and the linear + quadratic trend. A significant improvement was observed including the quadratic trend on each participant.

	pRF center (mm)	pRF surround (mm)	pRF center, linear and quadratic trends	pRF surround, linear and quadratic trends
Participant 1	0.62 < 1.31 < 1.86	0.47 < 1.34 < 1.80	R^2 (linear) = 1% R^2 (linear + quadratic) = 56% Anova test: F = 21.62, $p < 0.001$	R^2 (linear only) = 30% R^2 (linear + quadratic) = 48% Anova test: F = 6.03, $p < 0.05$
Participant 2	0.98 < 1.22 < 1.39	1.09 < 1.35 < 1.52	R^2 (linear only) = 7% R^2 (linear + quadratic) = 96% Anova test: F = 435.96, $p < 0.001$	R^2 (linear only) = 1% R^2 (linear + quadratic) = 98% Anova test: F = 387.89, $p < 0.001$
Participant 3	0.47 < 0.80 < 1.81	0.63 < 0.82 < 1.67	R^2 (linear only) = 1% R^2 (linear + quadratic) = 33% Anova test: F = 8.33, $p < 0.05$	R^2 (linear only) = 3% R^2 (linear + quadratic) = 56% Anova test: F = 20.69, $p < 0.001$
Participant 4	1.02 < 1.40 < 1.78	1.11 < 1.47 < 1.73	R^2 (linear only) = 7% R^2 (linear + quadratic) = 94% Anova test: F = 273.07, $p < 0.001$	R^2 (linear only) = 4% R^2 (linear + quadratic) = 97% Anova test: F = 531.03, $p < 0.001$

schemes, for example due to a larger inflow contribution with the short TR in the 2D EPI acquisition (Gao and Liu, 2012).

Local averaging and pRF scatter can explain pRF changes across cortical depth

The pRF properties, in particular center and surround size, increase from the middle of the cortical depth towards both superficial and deeper intra-cortical portions of V1. These two properties remain balanced across cortical depth as illustrated by the constant suppression index.

Can we explain the superficial and deeper intra-cortical pRF properties by summation of the pRFs of the central layers? Based upon the laminar information flow, we hypothesized that simple spatial summation of scattered pRFs from the central depths could yield pRF sizes similar to those seen in superficial and deeper locations. On the other hand, we have previously suggested that increased summation disrupts the center-surround pRF configuration (Zuiderbaan et al., 2012). Consequently, disruption of the center-surround configuration due to summation would need external influences to maintain the balance we observe. The last hypothesis suggests that spatial summation of the central layers cannot explain the pRF profile.

To dissociate between these hypotheses, we simulated whether we can recreate the pRFs at the superficial and deeper locations, based on a summation of the pRFs at the middle of the cortical depth. PRF properties at the middle of the cortical depth were summed at a range of positions (scatter). We repeated this procedure 2000 times, using bootstrapped samples of pRF center, surround, and the associated %BOLD amplitude from values obtained for the middle of the cortical depth (>1 mm and <1.5 mm from the GM/WM border; mean = 1.25 mm from the GM/WM border).

We used the estimates of pRF center, pRF surround, and the two associated %BOLD response amplitudes to recreate the DoG pRF. PRF DoG was expressed with the sum of two separated Gaussians: a positive amplitude Gaussian, with center pRF size as sigma and positive %BOLD (with respect to the mean, see Fig. 5) as amplitude, and a negative amplitude Gaussian, with surround pRF size as sigma and negative %BOLD (with respect to the mean, see Fig. 5) as amplitude, (one exemplar DoG pRF is represented in Fig. 9A, continuous black line; pRF center and surround size estimates for pRFs located at a cortical depth of 1.25 mm are reported in Fig. 9B & C). This pRF was scattered 20,000 times and averaged. Scattered pRF centers were extracted from a Gaussian distribution with center 0 and standard deviation of ½ pRF size, as reported in literature (Hetherington and Swindale, 1999). The pRF center and pRF surround estimates of the resulting (scattered) DoG were estimated using the R software implementation of non-linear least squares. Median and 95% confidence interval of the resulting pRF center and pRF surround sizes were derived and compared with those obtained from the data collected towards the pial surface (1.8 to 2.1 mm from GM/WM,

mean = 1.9 mm from the GM/WM border) or towards the GM/WM surface (0.2 to 0.7 mm from GM/WM, mean = 0.45 mm from the GM/WM border) from the mean profiles reported in Fig. 7A & B.

Results of our simulations show that spatial summation of the central pRFs can result in comparable pRFs we observe in deeper and superficial layers. In other words, the center-surround configuration of the pRF is still preserved (Fig. 9A), whereas it would be lost only for exceedingly big scatter values akin to our previous observation (Zuiderbaan et al., 2012). The extent of spatial summation is comparable to the level of scatter reported in the literature (~½ pRF size, Hetherington and Swindale, 1999).

Furthermore, the median and 95% confidence interval values obtained from our simulation are not significantly different from the average center and surround pRF sizes observed at 1.9 mm and 0.45 mm with respect to the GM/WM border, suggesting that a laminar hierarchy from middle to superficial and deeper intra-cortical portions of V1 can explain the U shaped function that characterizes pRF size across cortical depth.
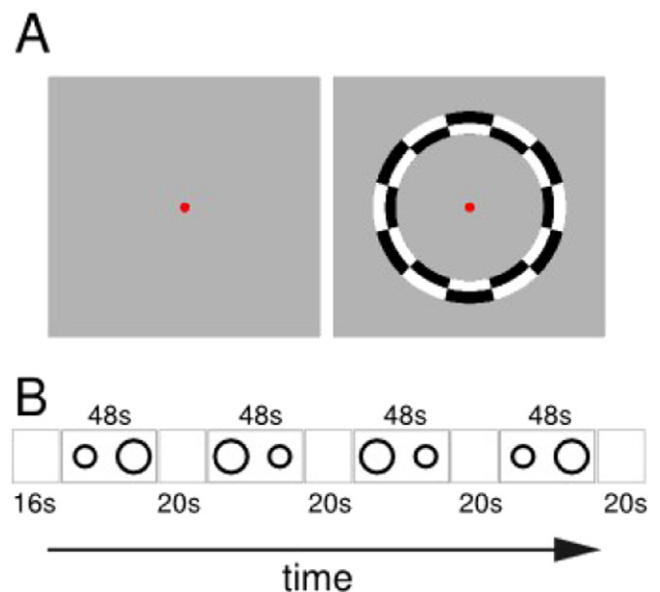
Fig. 1. Illustration of the stimuli for reconstructing pRF properties across cortical depth. Panel A: mean luminance stimulus and ring stimulus. Panel B: representation of stimuli time course during a single run: mean luminance for 16 s, ring expansion in 12 steps (0.5 degrees of visual angle with a stepsize of 0.25 degrees of visual angle, 48 s), mean luminance for 20 s, ring contraction (48 s), mean luminance (20 s), ring contraction (48 s), mean luminance (20 s), ring expansion (48 s) and then mean luminance (20 s).
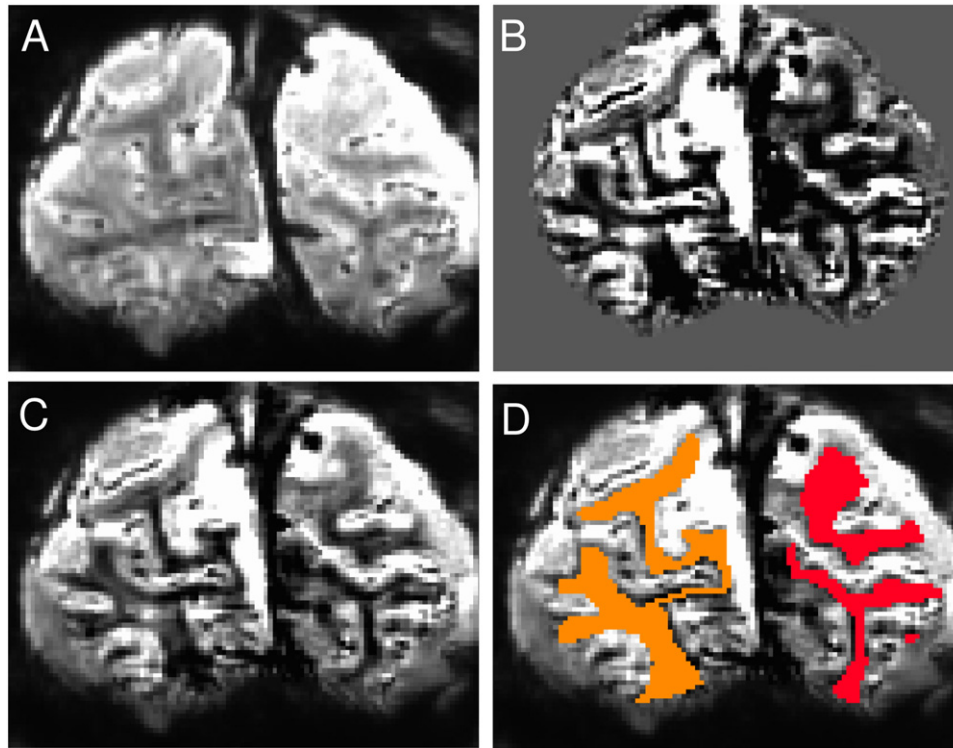
Fig. 2. Amplitude and phase-unwrapped functional images. Panel A, coronal slice from the mean motion corrected 3D-EPI amplitude volume. Panel B, coronal slice from the mean phase-unwrapped and motion corrected 3D-EPI phase volume. Panel C, coronal slice from a weighted sum of mean 3D-EPI amplitude and mean 3D-EPI phase volume. Panel D, same image as in panel C, with the manual segmentation superimposed (orange = left hemisphere, red = right hemisphere). The combination of amplitude and phase reveals enhanced anatomical detail and a good GM/WM contrast.

Discussion

Result summary

We acquired human sub-millimeter fMRI data at 7 Tesla and took advantage of the level of anatomical detail preserved in high-resolution (0.7 mm isotropic) T2*-weighted volumes as well as unwrapped T2*-weighted phase images to perform GM/WM segmentation directly on the fMRI phase images.

The cortical depth profile of center and surround pRF size estimates shows a U-shaped function across cortical depth. In contrast, the FWHM values of the hemodynamic response function that was derived from an independent scan show a monotonic increase across cortical depth, as well as an increase in %BOLD signal change, as previously reported in literature (Siero et al., 2011, Fig. 8). Hence the characteristic U-shaped

function of the pRF size profile across cortical depth cannot be explained by systematic changes of the HRF FWHM across cortical depth. The different trend between FWHM and pRF size across cortical depth is important since the FWHM of the hemodynamic response function can represent one of the major sources of bias in accurate pRF size estimation, as reported previously (Dumoulin and Wandell, 2008).

Methodological considerations

Segmentation

High resolution imaging aiming to characterize activity across cortical depth needs a very accurate GM/WM segmentation. Typically, this segmentation is performed on a separate anatomical volume and then projected onto the functional data after alignment. This procedure however can result in local misalignment due to inherently different local
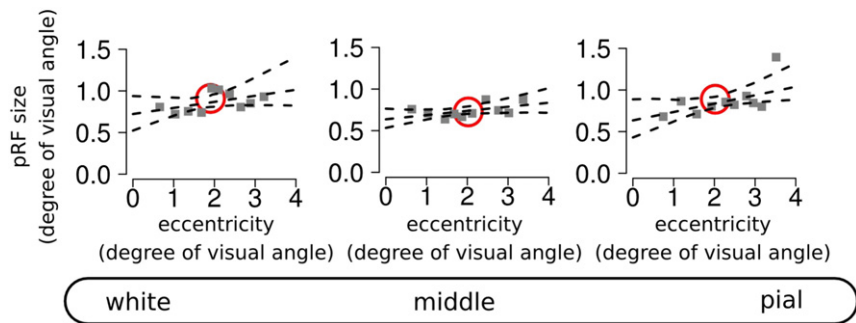
Fig. 3. pRF estimation across cortical depth, data reported from one participant for illustration purposes. pRF size scales linearly with eccentricity across V1. To account for the eccentricity covariate, selected voxels were binned in 10 points according to 10% percentiles of Euclidean distance from GM/WM surface (only 3 bins are shown in the example). The pRF × eccentricity linear relation was fit using standard GLM, separately for each Euclidean distance bin, in order to derive the line equation estimating the intercept and the slope. The dashed lines represent bootstrapped 95% quantiles and the median of the fit. The pRF size at 2° visual angle eccentricity was taken as the pRF size estimate for the corresponding Euclidean distance bin (red circle). The 10 pRF size estimates across the Euclidean distance bins constituted the pRF size profile across cortical depth.
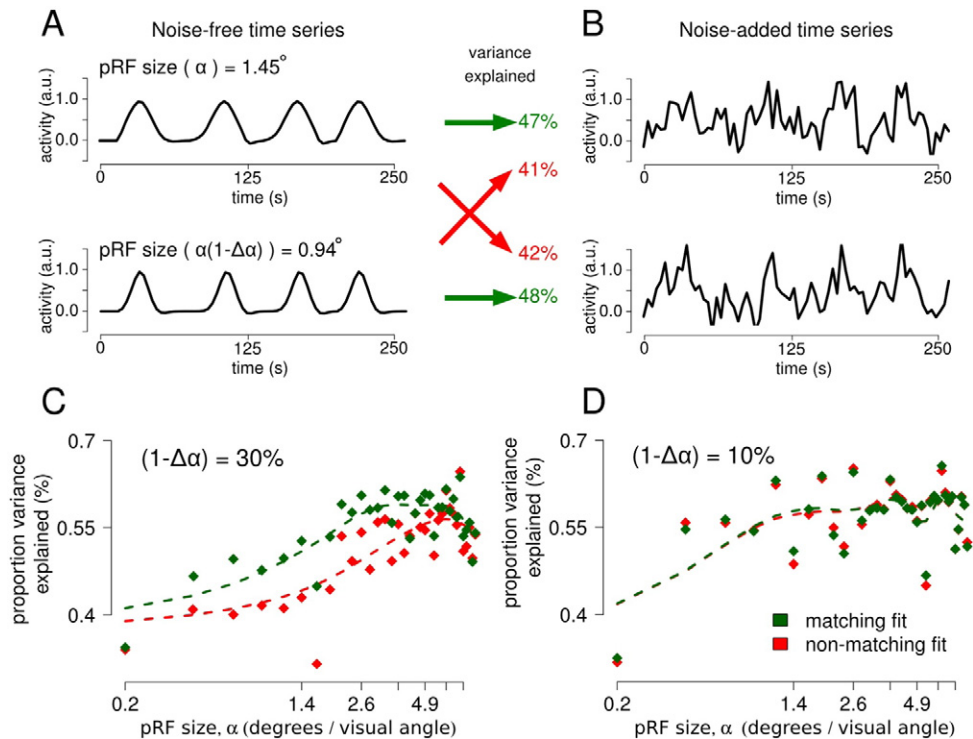
Fig. 4. pRF size estimation sensitivity. Panel A, noise-free time series with pRF size of 1.45 and 0.94 degrees of visual angle. Panel B, noise-added time series, obtained adding i.i.d noise. The green arrows represent matching linear regression fits and the corresponding variance explained. Red arrows represent non-matching linear regression fits and the corresponding variance explained. Panel C, proportion of variance explained as a function of pRF size for matching and non-matching fits when the 2 pRF differed in size by 30%. The matching variance explained is larger than the non-matching variance explained for a range between 0.4 and 4 degrees of visual angle. In this range, the technique adopted could correctly assign each pRF size estimate to each noise-added time series. Panel D, proportion of variance explained as a function of pRF size for matching and non-matching fits when the 2 pRF differed in size by 10%. In this case figure the matching variance explained is not different from the non-matching variance explained; given the small difference between pRF sizes (10%) the technique cannot correctly assign each pRF size estimate to each noise-added time series, and the estimates are confounded, showing the limit of the estimation technique.

distortions between functional and anatomical volumes. Further, this procedure can alter the resolution of the functional data (or the segmentation-based anatomy) due to the interpolation employed to align functional and anatomical volumes. Decreasing the level of interpolation at preprocessing steps is crucial to maintain the level of detail as similar as possible to the original acquisition resolution. We took advantage of recent evidence showing considerable amount of anatomical detail on unwrapped T2*-weighted phase images, (see Fig. 2, Abduljalil et al., 2003; Haacke et al., 2004; Duyn et al., 2007; Petridou et al., 2010) and performed manual segmentation directly on each participant's functional volumes, in the T2*-weighted EPI space. In this way we obtained an accurate GM/WM segmentation preserving the original acquisition resolution.

Segmenting directly the EPI space is a novel approach in ultra-high resolution imaging that overcomes the problem of realigning functional volumes to the anatomical space, thus decreasing the possibility of local errors in the realignment process that can severely affect the subsequent cortical depth analysis.

There is a considerable amount of anatomical detail in the unwrapped T2*-weighted phase images. Recent reports (Langkammer et al., 2012) show that phase contrast between cortical gray and white matter (despite their small difference in iron content) can be mainly attributed to variations in myelin content in the white matter, counteracting the effects of iron. U-fibers hug the gray-white interface and are known to have high iron concentration, and this could partially confuse the identification of the GM/WM boundary. We
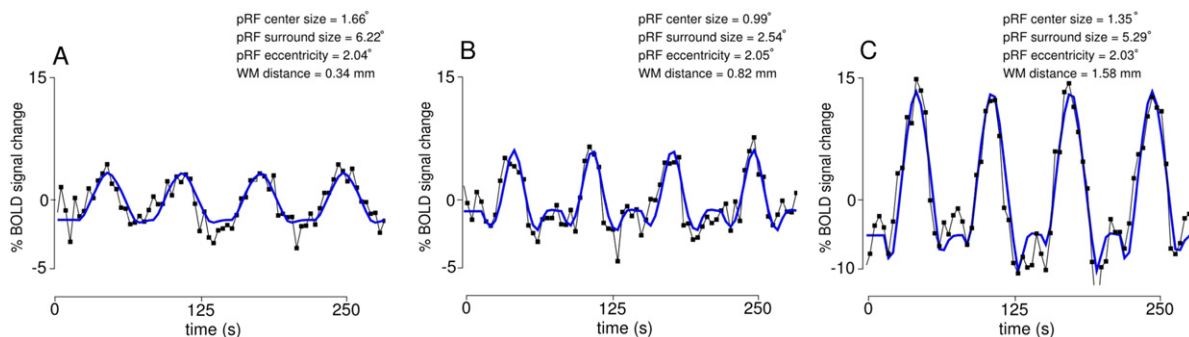
Fig. 5. %BOLD time courses from three voxels in V1, at 3 different distances from the GM/WM border and comparable eccentricity. Best least-squares fit (blue line) is superimposed on the raw data (white squares). Panel A, time course from a voxel at 0.34 mm from the GM/WM border; panel B, time course from a voxel at 0.82 mm from the GM/WM border; panel C, time course from a voxel at 1.58 mm from the GM/WM border. Even though the eccentricity estimate is comparable between the three voxels, pRF size varies across cortical depth, with larger pRF center sizes close to the GM/WM border and the pial surface (1.68 and 1.39 degrees of visual angle, respectively) as compared to intermediate positions (0.95 degrees of visual angle).
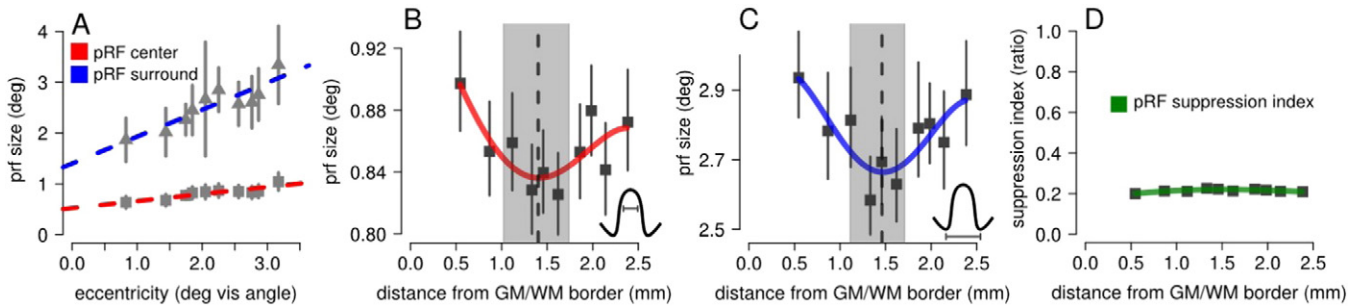
Fig. 6. Center and surround size estimates in primary visual cortex from a single participant. Panel A, the relationship between pRF center size and eccentricity in V1, pRF size increased with eccentricity. Error bars represent 95% CI from 2000 bootstrapped samples. Panel B, the relationship between pRF center size and distance from the GM/WM border. PRF center size estimates follow a U-shaped function, with larger pRF center size estimates close to the GM/WM border and the pial surface, compared to intermediate positions. Vertical dashed line represents the median location of the profile local minimum, gray area represents 95% CI, error bars represent 95% CI from 2000 bootstrapped samples. Panel C, the relationship between pRF surround size and distance from the GM/WM border. PRF surround size estimates again follow a U-shaped function, with larger pRF surround size estimates close to the GM/WM border and the pial surface, compared to intermediate positions. Vertical dashed line represents the median location of the profile local minimum, gray area represents 95% CI, error bars represents 95% CI from 2000 bootstrapped samples. Panel D, suppression index (see Eq. (2)) as a function of distance from the GM/WM border remains constant, around ~0.2 for this participant. Error bars represents 95% CI from 2000 bootstrapped samples.

compared the GM/WM segmentation of the 3D-EPI space to that obtained from a high-resolution T1-weighted space (see Supplementary material, Fig. 1) showing good correspondence between the two.

Spatial resolution

The extremely high nominal resolution (0.7 mm isotropic) at which we acquired the data allow us to reconstruct cortical depth profiles of BOLD % signal change and pRF size. However, the spatial resolution may change as a function of cortical depth as well (Polimeni et al., 2010). The latter effect is likely driven by the orthogonal orientation of the larger vasculature with respect to cortical surface (Duvernoy et al., 1981) and the consequent draining of de-oxygenated blood from the small capillaries towards the pial surface where large-diameter draining veins dominate the BOLD signal contribution (Fig. 8A, see Supplementary material, Figs. 5–10 for an evaluation of partial volume effects and noise on pRF size estimates). Furthermore, the nominal resolution is

affected by a number of factors that decrease the effective spatial resolution of the data, e.g. BOLD point spread function (Shmuel et al., 2007; Engel et al., 1997) and subject motion. Due to the vasculature arrangement across cortical depth and the limitations of the effective resolution, we do not present our profiles as separated into isolated laminar compartments, rather we show the progression of %BOLD signal change and pRF size continuously as a function of cortical depth. Therefore, the results shown are based on interpolation.

pRF estimates across cortical depth

The simulation presented in Fig. 4 shows that a certain degree of uncertainty for pRF size estimates is present at the single voxel level. If the fitting of the pRFs has a given uncertainty, then it can be argued that this is a source of estimation uncertainty that might affect the overall shape of the obtained profile. We address this concern by simulating a noise-free pRF size profile across cortical depth using an increasing number of voxels and adding uniform noise (equal to 15% of pRF size) and
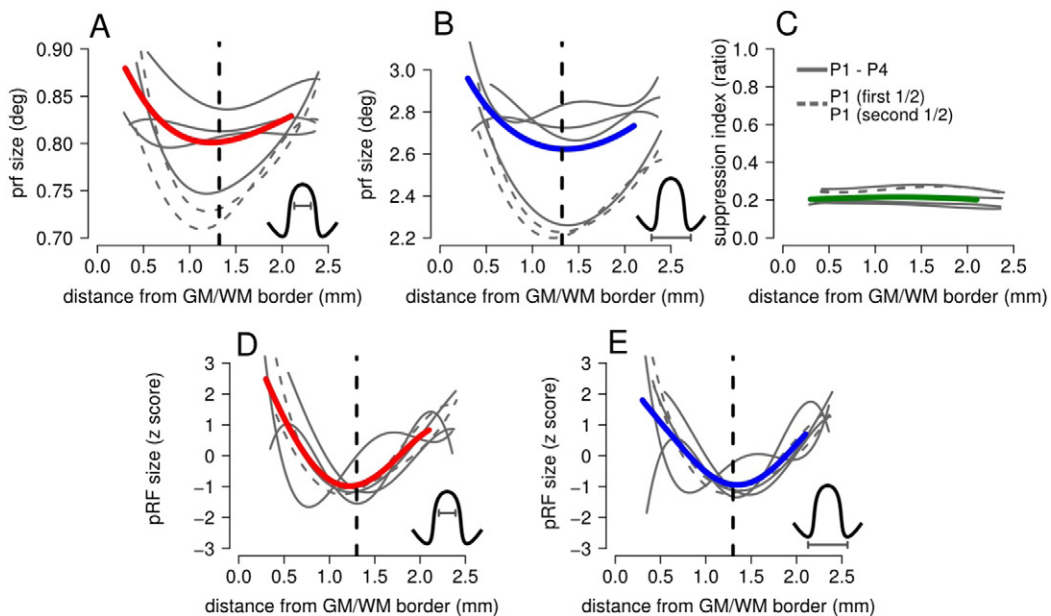
Fig. 7. Center, surround and suppression index estimates in V1. Panel A. the relationship between pRF center size and distance from GM/WM for all participants (gray continuous lines), test–retest (gray dashed lines) and average across participants (red line). Panel B. the relationship between pRF surround size and distance from GM/WM for all participants, test–retest and average across participants (blue line). Panel C. Suppression index as a function of distance from the GM/WM border for all participants, test–retest and average across participants (green line). A value of 0.5 indicates that suppression strength is equal to half of that of excitation in the center. Panels D and E, same as panels A, B but data was normalized with z-scores which highlights the same trend in all participants and in the test–retest datasets.
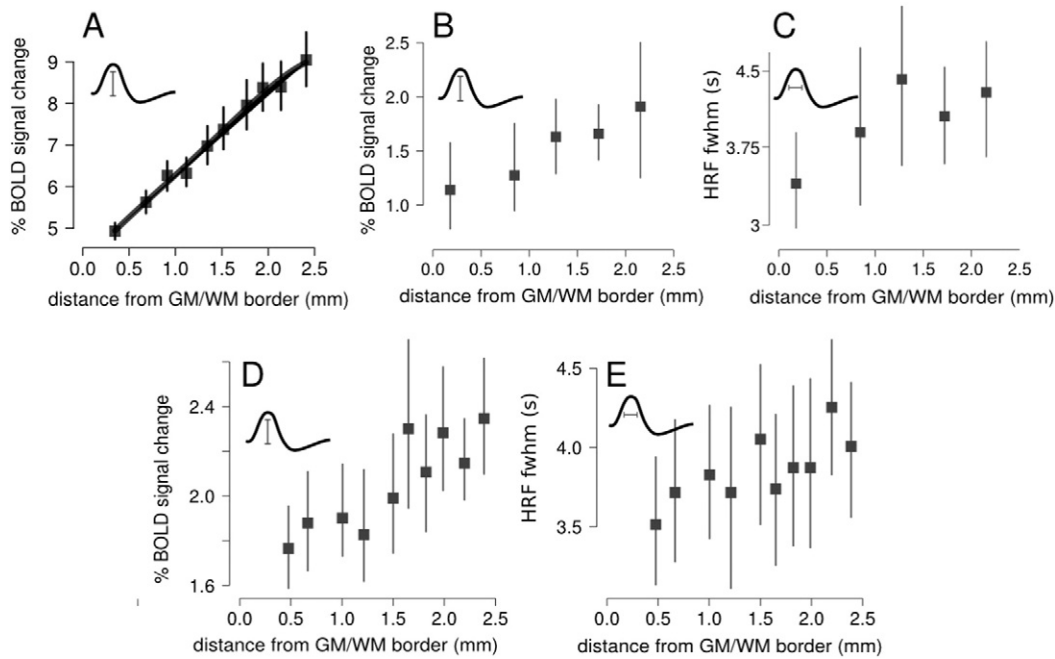
Fig. 8. %BOLD signal from pRF analysis and HRF estimates from an independent session. Panel A, %BOLD signal change across cortical depth from the 3D-EPI data used to estimate pRF size (single participant data, resolution = 0.7 mm isotropic, extracted from the same data reported in Fig. 6), error bars represent 95% CI from 2000 bootstrapped samples. Panel B, %BOLD signal change across cortical depth from the same participant, based on the multi-slice EPI data used to estimate the HRF (1.3 mm isotropic, temporal resolution = 0.85 s). Also in this case %BOLD signal increases towards the pial surface. Error bars represent 95% CI from 2000 bootstrapped samples. Panel C, same dataset as in panel B, in this case the plot shows the HRF FWHM across cortical depth, showing an increase in FWHM towards the pial surface. Error bars represent 95% CI from 2000 bootstrapped samples. Panels D, same results reported in panels B & C, but in this case the HRF was estimated from the 3D-EPI sequence (TR = 4 s), with a briefly presented, time jittered, visual stimuli. Also in this case error bars represent 95% CI from 2000 bootstrapped samples. Panel E, same dataset as in panel B, in this case the plot shows the HRF FWHM across cortical depth, showing an increase in FWHM towards the pial surface. Error bars represent 95% CI from 2000 bootstrapped samples.

Gaussian noise to the resulting pRF size (see Supplementary material, Fig. 6). The results of the simulation show that the uncertainty associated with each single voxel estimate does not bias the profile in any specific direction, and that the pRF profile can be recovered, provided that enough voxels are present for each cortical depth level (see Supplementary material, Fig. 6).

It might be hypothesized that the 'true' pRF size increases across cortical depth, simply following the BOLD signal increase across cortical depth, increasing towards the pial surface, where relatively large veins can be found (see Fig. 8, panel A). Given this scenario it may be possible that the noise distribution along cortical depth might have biased the pRF estimates towards the observed U-shaped trend. We address this issue by simulating a range of possible pRF size increases across cortical depth, reading out the resulting pRF size given the variance explained value associated with a given cortical depth value. The results of this simulation show that there is a simple additive shift between to the
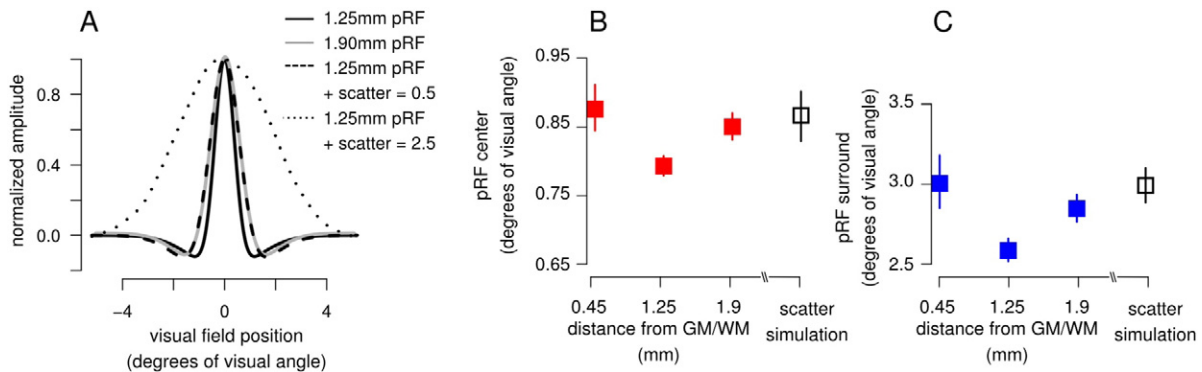
Fig. 9. Influence of scatter on pRF center and surround. Panel A, black continuous line represents the average pRF, 1.25 mm from the GM/WM border (derived from the average pRF profile across cortical depth, see Fig. 7, panel A, red line), gray continuous line represents the average pRF, 1.9 mm from the GM/WM border, dashed line represents the resulting pRF from averaging 20,000 pRFs at a cortical depth of 1.25 mm but with field position scattered, extracted from a Gaussian distribution with mean = 0 and sd = 0.5 ∗ pRF size. The center-surround configuration is well preserved, but both center and surround parameters are larger than the original standard pRF parameters. Dotted line represents the same pRF but with an unrealistically large scatter of 2.5 ∗ pRF size. In this case the center-surround configuration is lost. Panel B, median and 95% CI of pRF center estimates at 0.45 mm, 1.25 mm and 1.9 mm from the GM/WM border, derived from the average pRF profile across cortical depth, see Fig. 7, panel A (red line). The estimates obtained at 0.45 mm and 1.9 mm are not significantly different from a scattered version of the estimate obtained at 1.25 mm, with sd = 0.5 ∗ pRF size. Panel C, median and 95% CI of pRF surround estimates at 0.45 mm, 1.25 mm and 1.9 mm from the GM/WM border, derived from the average pRF profile across cortical depth, see Fig. 7, panel B (blue line). Also in this case the estimates obtained at 0.45 mm and 1.9 mm are not significantly different from a scattered version of the estimate obtained at 1.25 mm, with sd = 0.5 ∗ pRF size. These results suggest that a laminar hierarchy from middle to superficial and deeper intra-cortical portions of primary visual cortex can explain the U shaped function that characterizes the pRF size across cortical depth.

hypothesized increase pRF size across depth (see Supplementary material, Fig. 7).

fMRI and neurophysiology

The cortical depth profile of center and surround pRF size estimates shows a U-shaped function. We believe that this is largely consistent with invasive non-human neurophysiology. Neurophysiology in non-primate mammals describes a similar U-shaped RF size variation across cortical depth (Chapin, 1986; Vaiceliunaite et al., 2013; Self et al., 2014). On the other hand, in non-human primates a U-shaped RF size variation across cortical layers is not as clear as in non-primate mammals. Hubel and Wiesel (1972, 1977) suggest that there is a correlation between complexity and layering, where the cells in input layers tend to be least complex with smaller RFs. Sceniak et al. (2001) and Shushruth et al. (2009) report approximately constant RF sizes across lamina, though, in line with our results, they do report larger RF sizes in layer 6. Regarding pRF surround non-human primate neurophysiology shows larger extra-classical RF surrounds outside input layer 4 in primary visual cortex, a finding compatible with our results (Shushruth et al., 2009; Angelucci et al., 2002). Furthermore, absolute pRF center size estimates (~0.8 degree of visual angle) and pRF surround size estimates (~2.7 degree of visual angle) are remarkably similar to measures obtained from V1 recordings in non-human primate neurophysiology (Gattass et al., 1987; Rosa et al., 1988; Sceniak et al., 2001). We analyzed the sensitivity of the pRF estimation technique adopted here, in order to understand whether this fMRI to neurophysiology similarity reflects a true property of the underlying neuronal population, or whether it is just an epiphenomenon due to the methods adopted (as for example, a floor effect of the technique, with the measured values being just the smallest possible estimates that can be derived). Population receptive field sizes are affected by at least two relevant neural components, i.e. average single neuron RF size and RF positional scatter (Dumoulin and Wandell, 2008). Our data cannot distinguish either contribution. However, data from neurophysiology suggests that RFs size and RFs scatter are proportional (Hetherington and Swindale, 1999; Hubel and Wiesel, 1972).

Nevertheless, in order to answer this question we estimated the sensitivity of the pRF implementation adopted here across a range of potential pRF sizes, for a single voxel scenario. Simulation results show that we can reliably tell apart a single pRF with size ranging between ~0.4 degrees of visual angle to ~4 degrees of visual angle from a second pRF that is 30% smaller in size with respect to the former. This represents a biologically plausible rate, and is compatible with pRF size differences across lamina reported in literature (Chapin, 1986).

The observed estimates of ~0.8 degree of visual angle for pRF center and ~2.7 degrees of visual angle for pRF surround are well within the sensitivity boundaries of the technique adopted, thus these estimates are likely to reflect the real underlying neuronal population.

Processing across cortical depth

Neurophysiological results suggest a specific processing across lamina. First, lateral geniculate axons reach primary visual cortex at the level of layer 4C (Hubel and Wiesel, 1977). At this stage of processing neurons are strictly monocular (Hubel and Wiesel, 1972). After the first synaptic activity, horizontal and vertical connections rapidly distribute the signals across supra- and infra-granular layers (Sincich and Horton, 2005). Self et al. (2013) demonstrated that visual responses can be detected in the granular layer of primary visual cortex as early as ~40 ms after stimulus onset, rapidly followed by responses in infra- and supra-granular layers. Furthermore, it is also known that extra-striate afferents in primary visual cortex mediate extra-classical receptive field effects that are outside the range of horizontal connections inside V1, predominantly targeting infra- and supra-granular layers (Angelucci et al., 2002).

Our simulation suggests that pRF properties of superficial and deeper intra-cortical portions can be derived from summation of pRFs from the middle of cortical depth. Therefore, our data suggest that extra-striate afferents are not required to explain the pRF size and surround variation across cortical depth. The summation of pRFs in the middle of the cortical depth may reflect random position scatter of neuronal visual field encoding or may reflect an extended sampling of the middle of cortical depth analogous to pRF size changes across the visual field map hierarchy (Haak et al., 2013). Our simulation shows that adopting a level of scatter that is comparable to neurophysiological measurements (~½ RF size, Blakemore and Pettigrew, 1970; Hubel and Wiesel, 1972; Hetherington and Swindale, 1999) yields center surround configurations that are sufficient to explain the observed pRF properties in superficial and deeper intra-cortical portions (Fig. 9). The field-of-view adopted in our acquisition and the visual stimuli were specifically designed to target primary visual cortex, so we refrain from making claims about other areas in the visual hierarchy (as V2 and V3).

Conclusions

The cortical depth profile of center and surround pRF size estimates in human V1 shows a U-shaped function and balanced center-surround configuration across cortical depth. Our experimental results and simulations suggest that this pattern can be linked to the flow of signals from the granular layer of primary visual cortex to supra- and infra-granular layers by the intracortical connections after the first synapse (Sincich and Horton, 2005).

From a neuroimaging perspective, these results imply that a targeted experimental design allows investigation of aspects of cortical depth processing that are orthogonal to the prominent influence of vasculature across cortical depth. These computational neuroimaging designs are able to derive features that are independent from the large %BOLD signal gradient towards the pial surface as well as other haemodynamic parameters (as FWHM), allowing to bridge the gap between neurophysiology and neuroimaging literature.

Conflict of interest

None.

Appendix A. Supplementary data

Supplementary data to this article can be found online at http://dx.doi.org/10.1016/j.neuroimage.2016.06.048.

References

Abduljalil, A.M., Schmalbrock, P., Novak, V., Chakeres, D.W., 2003. Enhanced gray and white matter contrast of phase susceptibility-weighted images in ultra-high-field magnetic resonance imaging. J. Magn. Reson. Imaging 18, 284–290.

Allman, J., Miezin, F., McGuinness, E., 1985. Stimulus specific responses from beyond the classical receptive field: neurophysiological mechanisms for local-global comparisons in visual neurons. Annu. Rev. Neurosci. 8, 407–430.

Amano, K., Wandell, B.A., Dumoulin, S.O., 2009. Visual field maps, population receptive field sizes, and visual field coverage in the human MT+ complex. J. Neurophysiol. 102, 2704–2718.

Angelucci, A., Levitt, J.B., Walton, E.J.S., Hupe, J.-M., Bullier, J., Lund, J.S., 2002. Circuits for local and global signal integration in primary visual cortex. J. Neurosci. 22, 8633–8646.

Bilgic, B., Fan, A.P., Polimeni, J.R., Cauley, S.F., Bianciardi, M., Adalsteinsson, E., Wald, L.L., Setsompop, K., 2014. Fast quantitative susceptibility mapping with L1-regularization and automatic parameter selection. Magn. Reson. Med. 72, 1444–1459.

Blakemore, C., Pettigrew, J.D., 1970. Retinal disparity and retinal dominance of binocular cortical neurones. J. Physiol. 210, 157P–159P.

Brainard, D.H., 1997. The psychophysics toolbox. Spat. Vis. 10, 433–436.

Burock, M.A., Buckner, R.L., Woldorff, M.G., Rosen, B.R., Dale, A.M., 1998. Randomized event-related experimental designs allow for extremely rapid presentation rates using functional MRI. Neuroreport 9, 3735–3739.

Callaway, E.M., 1998. Local circuits in primary visual cortex of the macaque monkey. Annu. Rev. Neurosci. 21, 47–74.

Cavanaugh, J.R., Bair, W., Movshon, J.A., 2002. Nature and interaction of signals from the receptive field center and surround in macaque V1 neurons. J. Neurophysiol. 88, 2530–2546.

Chapin, J.K., 1986. Laminar differences in sizes, shapes, and response profiles of cutaneous receptive fields in the rat SI cortex. Exp. Brain Res. 62, 549–559.

Chen, G., Wang, F., Gore, J.C., Roe, A.W., 2013. Layer-specific BOLD activation in awake monkey V1 revealed by ultra-high spatial resolution functional magnetic resonance imaging. NeuroImage 64, 147–155.

De Martino, F., Zimmermann, J., Muckli, L., Ugurbil, K., Yacoub, E., Goebel, R., 2013. Cortical depth dependent functional responses in humans at 7 T: improved specificity with 3D GRASE. PLoS One 8 (3), e60514.

DeYoe, E.A., Carman, G.J., Bandettini, P., Glickman, S., Wieser, J., Cox, R., Miller, D., Neitz, J., 1996. Mapping striate and extrastriate visual areas in human cerebral cortex. Proc. Natl. Acad. Sci. U. S. A. 93, 2382–2386.

Dumoulin, S.O., Wandell, B.A., 2008. Population receptive field estimates in human visual cortex. NeuroImage 39, 647–660.

Duvernoy, H.M., Delon, S., Vannson, J.L., 1981. Cortical blood vessels of the human brain. Brain Res. Bull. 7, 519–579.

Duyn, J.H., van Gelderen, P., Li, T.-Q., de Zwart, J.A., Koretsky, A.P., Fukunaga, M., 2007. High-field MRI of brain cortical substructure based on signal phase. Proc. Natl. Acad. Sci. U. S. A. 104, 11796–11801.

Engel, S.A., Rumelhart, D.E., Wandell, B.A., Lee, A.T., Glover, G.H., Chichilnisky, E.J., Shadlen, M.N., 1994. fMRI of human visual cortex. Nature 369, 525.

Engel, S.A., Glover, G.H., Wandell, B.A., 1997. Retinotopic organization in human visual cortex and the spatial precision of functional MRI. Cereb. Cortex 7 (2), 181–192.

Fedorov, A., Beichel, R., Kalpathy-Cramer, J., Finet, J., Fillion-Robin, J.-C., Pujol, S., Bauer, C., Jennings, D., Fennessy, F., Sonka, M., Buatti, J., Aylward, S., Miller, J.V., Pieper, S., Kikinis, R., 2012. 3D Slicer as an image computing platform for the Quantitative Imaging Network. Magn. Reson. Imaging 30, 1323–1341.

Felleman, D.J., Van Essen, D.C., 1987. Receptive field properties of neurons in area V3 of macaque monkey extrastriate cortex. J. Neurophysiol. 57, 889–920.

Fracasso, A., van Veluw, S.J., Visser, F., Luijten, P.R., Spliet, W., Zwanenburg, J.J., Dumoulin, S.O., Petridou, N., 2016. Lines of Baillarger in vivo and ex vivo: myelin contrast across lamina at 7 T MRI and histology. NeuroImage 133, 163–175 (Jun 30).

Friston, K.J., Fletcher, P., Josephs, O., Holmes, A., Rugg, M.D., Turner, R., 1998. Event-related fMRI: characterizing differential responses. NeuroImage 7, 30–40.

Gao, J.H., Liu, H.L., 2012. Inflow effects on functional MRI. NeuroImage 62 (2), 1035–1039.

Gattass, R., Sousa, A.P.B., Rosa, M.G.P., 1987. Visual topography of V1 in the Cebus monkey. J. Comp. Neurol. 259, 529–548.

Glover, G.H., 1999. Deconvolution of impulse response in event-related BOLD fMRI. NeuroImage 9, 416–429.

Glover, G.H., Li, T.Q., Ress, D., 2000. Image-based method for retrospective correction of physiological motion effects in fMRI: RETROICOR. Magn. Reson. Med. 44, 162–167.

Goense, J.B.M., Logothetis, N.K., 2006. Laminar specificity in monkey V1 using high-resolution SE-fMRI. Magn. Reson. Imaging 24, 381–392.

Goense, J.B.M., Zappe, A.-C., Logothetis, N.K., 2007. High-resolution fMRI of macaque V1. Magn. Reson. Imaging 25, 740–747.

Goense, J., Merkle, H., Logothetis, N.K., 2012. High-resolution fMRI reveals laminar differences in neurovascular coupling between positive and negative BOLD responses. Neuron 76, 629–639.

Haacke, E.M., Brown, R.W., Thompson, M.R., Venkatesan, R., 1999. Magnetic Resonance Imaging: Physical Principles and Sequence Design. John Wiley and Sons, New York.

Haacke, E.M., Xu, Y., Cheng, Y.-C.N., Reichenbach, J.R., 2004. Susceptibility weighted imaging (SWI). Magn. Reson. Med. 52, 612–618.

Haak, K.V., Winawer, J., Harvey, B.M., Renken, R., Dumoulin, S.O., Wandell, B.A., Cornelissen, F.W., 2013. Connective field modeling. NeuroImage 66C, 376–384.

Hagberg, G.E., Zito, G., Patria, F., Sanes, J.N., 2001. Improved detection of event-related functional MRI signals using probability functions. NeuroImage 14, 1193–1205.

Harel, N., Lin, J., Moeller, S., Ugurbil, K., Yacoub, E., 2006. Combined imaging—histological study of cortical laminar specificity of fMRI signals. NeuroImage 29, 879–887.

Harvey, B.M., Dumoulin, S.O., 2011. The relationship between cortical magnification factor and population receptive field size in human visual cortex: constancies in cortical architecture. J. Neurosci. 31, 13604–13612.

Hetherington, P.A., Swindale, N.V., 1999. Receptive field and orientation scatter studied by tetrode recordings in cat area 17. Vis. Neurosci. 16, 637–652.

Hubel, D.H., Wiesel, T.N., 1968. Receptive fields and functional architecture of monkey striate cortex. J. Physiol. 195, 215–243.

Hubel, D.H., Wiesel, T.N., 1972. Laminar and columnar distribution of geniculo-cortical fibers in the macaque monkey. J. Comp. Neurol. 146, 421–450.

Hubel, D.H., Wiesel, T.N., 1977. Ferrier lecture. Functional architecture of macaque monkey visual cortex. Proc. R. Soc. Lond. Ser. B Biol. Sci. 198, 1–59.

Huber, L., Goense, J., Kennerley, A.J., Ivanov, D., Krieger, S.N., Lepsien, J., Trampel, R., Turner, R., Möller, H.E., 2014. Investigation of the neurovascular coupling in positive and negative BOLD responses in human brain at 7 T. NeuroImage 97, 349–362.

Huber, L., Goense, J., Kennerley, A.J., Trampel, R., Guidi, M., Reimer, E., Ivanov, D., Neef, N., Gauthier, C.J., Turner, R., Möller, H.E., 2015. Cortical lamina-dependent blood volume changes in human brain at 7 T. NeuroImage 107, 23–33.

Jenkinson, M., Beckmann, C.F., Behrens, T.E.J., Woolrich, M.W., Smith, S.M., 2012. FSL. NeuroImage 62, 782–790.

Jin, T., Kim, S.G., 2008. Cortical layer-dependent dynamic blood oxygenation, cerebral blood flow and cerebral blood volume responses during visual stimulation. NeuroImage 43 (1), 1–9.

Kay, K.N., Naselaris, T., Prenger, R.J., Gallant, J.L., 2008. Identifying natural images from human brain activity. Nature 452, 352–355.

Koopmans, P.J., Barth, M., Norris, D.G., 2010. Layer-specific BOLD activation in human V1. Hum. Brain Mapp. 31 (9), 1297–1304.

Koopmans, P.J., Barth, M., Orzada, S., Norris, D.G., 2011. Multi-echo fMRI of the cortical laminae in humans at 7 T. NeuroImage 56 (3), 1276–1285.

Langkammer, C., Schweser, F., Krebs, N., Deistung, A., Goessler, W., Scheurer, E., Sommer, K., Reishofer, G., Yen, K., Fazekas, F., Ropele, S., Reichenbach, J.R., 2012. Quantitative susceptibility mapping (QSM) as a means to measure brain iron? A post mortem validation study. NeuroImage 62 (3), 1593–1599.

Miezin, F.M., Maccotta, L., Ollinger, J.M., Petersen, S.E., Buckner, R.L., 2000. Characterizing the hemodynamic response: effects of presentation rate, sampling procedure, and the possibility of ordering brain activity based on relative timing. NeuroImage 11, 735–759.

Nestares, O., Heeger, D.J., 2000. Robust multiresolution alignment of MRI brain volumes. Magn. Reson. Med. 43, 705–715.

Olman, C.A., Harel, N., Feinberg, D.A., He, S., Zhang, P., Ugurbil, K., Yacoub, E., 2012. Layer-specific fMRI reflects different neuronal computations at different depths in human V1. PLoS One 7, e32536.

Pelli, D.G., 1997. The VideoToolbox software for visual psychophysics: transforming numbers into movies. Spat. Vis. 10, 437–442.

Petridou, N., Wharton, S.J., Lotfipour, A., Gowland, P., Bowtell, R., 2010. Investigating the effect of blood susceptibility on phase contrast in the human brain. NeuroImage 50, 491–498.

Petridou, N., Italiaander, M., van de Bank, B.L., Siero, J.C.W., Luijten, P.R., Klomp, D.W.J., 2013. Pushing the limits of high-resolution functional MRI using a simple high-density multi-element coil design. NMR Biomed. 26, 65–73.

Pfeuffer, J., McCullough, J.C., de Moortele, P.F.V., Ugurbil, K., Hu, X., 2003. Spatial dependence of the nonlinear BOLD response at short stimulus duration. NeuroImage 18, 990–1000.

Polimeni, J.R., Fischl, B., Greve, D.N., Wald, L.L., 2010. Laminar analysis of 7 T BOLD using an imposed spatial activation pattern in human V1. NeuroImage 52 (4), 1334–1346.

Ress, D., Glover, G.H., Liu, J., Wandell, B., 2007. Laminar profiles of functional activity in the human brain. NeuroImage 34, 74–84.

Rosa, M.G.P., Sousa, A.P.B., Gattass, R., 1988. Representation of the visual field in the second visual area in the Cebus monkey. J. Comp. Neurol. 275, 326–345.

Sceniak, M.P., Hawken, M.J., Shapley, R., 2001. Visual spatial characterization of macaque V1 neurons. J. Neurophysiol. 85, 1873–1887.

Self, M.W., van Kerkoerle, T., Supèr, H., Roelfsema, P.R., 2013. Distinct roles of the cortical layers of area V1 in figure-ground segregation. Curr. Biol. 23, 2121–2129.

Self, M.W., Lorteije, J.A.M., Vangeneugden, J., van Beest, E.H., Grigore, M.E., Levelt, C.N., Heimel, J.A., Roelfsema, P.R., 2014. Orientation-tuned surround suppression in mouse visual cortex. J. Neurosci. 34, 9290–9304.

Sereno, M.I., Dale, A.M., Reppas, J.B., Kwong, K.K., Belliveau, J.W., Brady, T.J., Rosen, B.R., Tootell, R.B., 1995. Borders of multiple visual areas in humans revealed by functional magnetic resonance imaging. Science 268, 889–893.

Shmuel, A., Yacoub, E., Chaimow, D., Logothetis, N.K., Ugurbil, K., 2007. Spatio-temporal point-spread function of fMRI signal in human gray matter at 7 Tesla. NeuroImage 35 (2), 539–552.

Shushruth, S., Ichida, J.M., Levitt, J.B., Angelucci, A., 2009. Comparison of spatial summation properties of neurons in macaque V1 and V2. J. Neurophysiol. 102, 2069–2083.

Siero, J.C.W., Petridou, N., Hoogduin, H., Luijten, P.R., Ramsey, N.F., 2011. Cortical depth-dependent temporal dynamics of the BOLD response in the human brain. J. Cereb. Blood Flow Metab. 31, 1999–2008.

Silva, A.C., Koretsky, A.P., 2002. Laminar specificity of functional MRI onset times during somatosensory stimulation in rat. Proc. Natl. Acad. Sci. 99 (23), 15182–15187.

Sincich, L.C., Horton, J.C., 2005. The circuitry of V1 and V2: integration of color, form, and motion. Annu. Rev. Neurosci. 28, 303–326.

Vaiceliunaite, A., Erisken, S., Franzen, F., Katzner, S., Busse, L., 2013. Spatial integration in mouse primary visual cortex. J. Neurophysiol. 110, 964–972.

Waehnert, M.D., Dinse, J., Weiss, M., Streicher, M.N., Waehnert, P., Geyer, S., Turner, R., Bazin, P.-L., 2014. Anatomically motivated modeling of cortical laminae. NeuroImage 93 (Pt 2), 210–220.

Winawer, J., Horiguchi, H., Sayres, R.A., Amano, K., Wandell, B.A., 2010. Mapping hV4 and ventral occipital cortex: the venous eclipse. J. Vis. 10, 1.

Zhang, N., Zhu, X.-H., Chen, W., 2008. Investigating the source of BOLD nonlinearity in human visual cortex in response to paired visual stimuli. NeuroImage 43, 204–212.

Zimmermann, J., Goebel, R., De Martino, F., van de Moortele, P.-F., Feinberg, D., Adriany, G., Chaimow, D., Shmuel, A., Uğurbil, K., Yacoub, E., 2011. Mapping the organization of axis of motion selective features in human area MT using high-field fMRI. PLoS One 6, e28716.

Zuiderbaan, W., Harvey, B.M., Dumoulin, S.O., 2012. Modeling center-surround configurations in population receptive fields using fMRI. J. Vis. 12, 10.